Simulation of time- And frequency-resolved four-wave-mixing signals at finite temperatures: A thermo-field dynamics approach

Simulation of nonlinear femtosecond signals at finite temperature via Thermo Field Dynamics - Tensor Train method: General theory and application to time- and frequency-resolved fluorescence of the Fenna–Matthews–Olson complex

Maxim F. Gelin

School of Science, Hangzhou Dianzi University, Hangzhou 310018, China

Raffaele Borrelli

DISAFA, University of Torino, Grugliasco I-10095, Italy

Abstract

Addressing needs of contemporary nonlinear femtosecond optical spectroscopy, we have developed a fully quantum numerically-accurate wave-function-based approach for the calculation of third-order spectroscopic signals of polyatomic molecules and molecular aggregates at finite temperature. The approach is based on the Thermo Field Dynamics (TFD) representation of quantum mechanics and tensor-train (TT) machinery for efficient numerical simulation of quantum evolution of systems with many degrees of freedom. The developed TFD-TT approach is applied to the calculation of time- and frequency-resolved fluorescence spectra of the Fenna–Matthews–Olson (FMO) antenna complex at room temperature taking into account finite time-frequency resolution in fluorescence detection, orientational averaging, and static disorder.

Keywords: Thermo Field Dynamics; tensor trains, matrix product states, femtosecond spectroscopy, nonlinear response functions.

I. INTRODUCTIONS

Nonlinear femtosecond electronic spectroscopy is the main diagnostic tool for the detailed characterization of photophysical and photochemical processes in polyatomic chromophores and molecular aggregates in real time [1–7]. However, measured spectroscopic responses contain information on the system dynamics only implicitly, through the dependence of signals on carrier frequencies, delay times, phases, and temporal envelopes of the laser pulses. For example, time- and frequency-resolved fluorescence signal considered in the present work is triggered by a femtosecond pump pulse and is detected by mixing of spontaneous emission of excited electronic state(s) with a femtosecond up-conversion pulse [8, 9]. The signal depends on the time delay between the pump and up-conversion pulses, on carrier frequency and duration of the pump pulse, and on time- and frequency-resolution of the up-conversion setup. Since most of polyatomic molecules and notably molecular aggregates are complex multi-mode systems, theoretical support is indispensable for the extraction of the intrinsic system evolution from detected spectroscopic observables.

Until recently, theoretical simulations of nonlinear spectroscopic signals were based on phenomenological models with several relevant electronic states, a few optically-active vibrational modes, and oversimplified description of vibrational relaxation and optical dephasing. Computer simulations have revolutionized theoretical spectroscopy: It became possible to develop more complex and therefore more realistic models in which relevant potential energy surfaces and transition dipole moments were retrieved from electronic-structure calculations. Linear-vibronic-coupling (LVC) based approach, in which potential energy surfaces and transition dipole moments are represented by polynomials of nuclear coordinates, is one of the most popular and reliable methods for the construction of *ab initio*-based Hamiltonians of polyatomic chromophores [4, 10] and molecular aggregates [5, 6]. The LVC can also be efficiently interfaced with classical trajectory simulations [11]. Usually, LVC Hamiltonians contain high-frequency Franck-Condon-active vibrational modes (which are strongly coupled to electronic states and are responsible for vibronic structure of spectroscopic signals) as well as relevant low-frequency vibrational modes (which are weakly coupled to electronic states and are primarily responsible for vibrational relaxation and electronic dephasing). Since typical energies of low-frequency modes are comparable or less than thermal energy at ambient conditions, it is necessary to have a computationally efficient methodology for

the simulation of nonlinear femtosecond signals at finite temperature.

Wave-function-based-methods, notably the (multilayer) multi-configuration time-dependent Hartree (MCTDH) method [12] and the variational multi-configurational Gaussian (vMCG) method [13], are known to be highly efficient in numerically accurate simulation of multi-mode fully quantum dynamics driven by LVC Hamiltonians at zero temperature. In the late 1990s, this was impressively demonstrated on a 24-vibrational-mode model of pyrazine [14, 15]. Yet generalization of these methods to finite temperatures is computationally demanding and requires multidimensional statistical sampling of initial conditions [16–21]. Hence applications of the MCTDH method to the simulation of spectroscopic signals at finite temperatures are quite limited [17, 22–24]. The multiple variational Davydov *Ansatz* method, which was used to simulate nonlinear spectroscopic signals at zero temperature [25–30], was recently extended to finite temperatures [31] by employing the sampling technique of Refs. [32, 33]. However, the method of Ref. [31] is computationally efficient for LVC models with only a few low-frequency modes. There exist also approximate (though quite accurate for certain classes of multi-mode systems) finite-temperature methods of the simulation of spectroscopic signals of multi-mode systems by employing the thawed Gaussian *Ansatz* method [34–36] and quasiclassical mapping approaches [37–40].

Recently, we have developed a computationally efficient, fully quantum and numerically accurate wave-function-based method for the simulation of quantum dynamics of systems with many degrees of freedom at finite temperature [41–44]. The method is based on the ideas of Thermo Field Dynamics (TFD) [45–49] (which enables a finite temperature wave-function representation of quantum mechanics) and the tensor-train (TT) methodology [50–52]. In physics literature, it is common to use the name matrix product states (MPS) instead of TTs, and the methodology very similar to TFD-TT is called finite-temperature time-dependent density matrix renormalization group (TD-DMRG) [53]. Over the recent years, the TFD-TT machinery has been applied to the calculation of steady-state properties and signals of molecular systems at finite temperature [54–62]. In this work, the TFD-TT approach is extended towards the simulation of nonlinear response functions and electronic femtosecond spectroscopic signals.

To illustrate performance of the TFD-TT methodology, we simulate time- and frequency-resolved fluorescence of the Fenna–Matthews–Olson (FMO) complex. This antenna complex was extensively studied by femtosecond transient-absorption pump-probe spectroscopy [63,

64] and electronic two-dimensional spectroscopy [65–68] (see also recent reviews [69–71]). However, to our knowledge, no time- and frequency-resolved fluorescence signal of FMO was detected and no theoretical simulations of this signal were attempted – despite time- and frequency-resolved fluorescence reveals wavepacket dynamics exclusively in excited electronic states, without admixture of ground-state bleach and excited-state absorption.

Our paper is structured as follows. Sec. II contains a brief introduction to the TFD methodology for time-dependent LVC Hamiltonians. The explicit expressions for the TFD third-order nonlinear response functions are derived in Sec. III. Application of the TT methodology for the evaluation of nonlinear response functions is discussed in Sec. IV. Simulated time- and frequency-resolved signals for the FMO antenna complex are presented and discussed in Sec. V. Sec. VI contains the conclusions and the discussion of the future developments.

II. TFD METHODOLOGY

A. Starting equations

The third-order polarization $\mathcal{P}(t)$ in the appropriate phase-matching direction is the key quantity specifying nonlinear femtosecond signals [1–7]. It describes the third-order response of the molecular system to the electric field of relevant laser pulses. Once $\mathcal{P}(t)$ is known, any spectroscopic signal can be calculated. To evaluate $\mathcal{P}(t)$, we need calculate the response of the system (described by the Hamiltonian H) to electric fields of the relevant laser pulses (described by the interaction Hamiltonian $H_F(t)$). If the system is specified by the density matrix $\rho(t)$, the response can be obtained from the solution of the driven Liouville – von Neumann equation ($\hbar = 1$)

$$\partial_t \rho(t) = -i[H + H_F(t), \rho(t)]. \tag{1}$$

As has been explained in the Introduction, we assume that the system is characterized by a standard LVC excitonic Hamiltonian

$$H = \sum_n \varepsilon_n c_n^\dagger c_n - \sum_{n \neq m} J_{nm} c_n^\dagger c_m + \sum_k \omega_k a_k^\dagger a_k - \sum_{kn} \frac{g_{kn}}{\sqrt{2}} c_n^\dagger c_n (a_k^\dagger + a_k). \tag{2}$$

Here $c_n^\dagger$ (c_n) create (annihilate) electronic excitation in the state n and obey the Pauli commutation rules $[c_k, c_{k'}^\dagger] = \delta_{kk'}(1 - 2c_k^\dagger c_{k'})$, ε_n are site energies, J_{nm} are electronic couplings,

$a_n^\dagger$ (a) are the creation and annihilation operators of the kth harmonic mode with frequencies ω_k, and the parameters g_{nk} determine the strength of the electron-vibrational coupling. In the remainder of the present work we adopt excitonic notation and refer to the Hamiltonian of Eq. (2) as excitonic Hamiltonian [5, 6]. However the developed formalism is equally applicable to polyatomic chromophores [4, 10] and molecular aggregates [5, 6] described by LVC Hamiltonians.

The system-field interaction Hamiltonian is given by the expression [1–7]

$$H_F(t) = E(t)\hat{\mu}_+ + E^*(t)\hat{\mu}_- \tag{3}$$

where $E(t)$ is the total electric field of the relevant laser pulses,

$$\hat{\mu}_+ = \sum_n c_n^\dagger(\boldsymbol{s}\boldsymbol{\mu}_n), \;\; \hat{\mu}_- = \sum_n c_n(\boldsymbol{s}\boldsymbol{\mu}_n) \tag{4}$$

are the raising and lowering components of the transition dipole moment operator

$$\hat{\mu} = \hat{\mu}_+ + \hat{\mu}_-, \tag{5}$$

$\boldsymbol{\mu}_n$ are the transition dipole moment vectors, and $\boldsymbol{s}$ is the polarization of the laser pulses. Eq. (3) is written the rotating wave approximation. This approximation is thoroughly satisfied in femtosecond weak-field electronic nonlinear spectroscopy, since electronically-resonant transitions are relevant only [1].

We assume that the entire system is prepared at a certain time moment t_{in} before arrival of the laser pulses at thermal vibrational equilibrium in the electronic (excitonic) ground state $|g\rangle$. Hence the initial condition for the Liouville – von Neumann equation (1) reads

$$\rho(t_{in}) = |g\rangle\langle g|\rho_v, \tag{6}$$

where

$$\rho_v = Z_v^{-1} \exp\{-\beta \sum_k \omega_k a_k^\dagger a_k\}, \tag{7}$$

Z_v is the partition function, $\beta = (k_B T)^{-1}$, k_B is the Boltzmann constant, and T is the temperature. With the above definitions, the total nonlinear polarization can be evaluated as

$$\mathcal{P}(t) = \mathrm{Tr}\{\hat{\mu}\rho(t)\}. \tag{8}$$

B. TFD Schrodinger equation

The Liouville – von Neumann equation (1) is a standard departing point for the formal calculation of various spectroscopic signals [1–7]. Here, following the general scheme of Ref. [72], we demonstrate how Eq. (1) can be equivalently recast in the TFD representation.

Let us introduce the eigenvectors of the vibrational Hamiltonian,

$$\sum_l \omega_l a_l^\dagger a_l |\boldsymbol{k}\rangle = E_{\boldsymbol{k}} |\boldsymbol{k}\rangle.$$

Obviously,

$$|\boldsymbol{k}\rangle = \prod_l |k_l\rangle, \;\; E_{\boldsymbol{k}} = \sum_l k_l \omega_l \tag{9}$$

where $|k_l\rangle$ are the eigenvectors of the lth harmonic mode. We also define vectors $|\tilde{\boldsymbol{k}}\rangle$ which are a copy of the original vectors $|\boldsymbol{k}\rangle$ but act in a different Hilbert space, the so-called *tilde* space. Adopting the notation

$$|\boldsymbol{k}\tilde{\boldsymbol{k}}\rangle = |\boldsymbol{k}\rangle|\tilde{\boldsymbol{k}}\rangle,$$

we introduce the unity vector in the $|\boldsymbol{k}\rangle \otimes |\tilde{\boldsymbol{k}}\rangle$ vector space,

$$|\boldsymbol{I}_v\rangle = \sum_{\boldsymbol{k}} |\boldsymbol{k}\tilde{\boldsymbol{k}}\rangle, \tag{10}$$

and the the so-called thermal vacuum state,

$$|\mathbf{0}_v(\beta)\rangle = \sqrt{\rho_v}|\boldsymbol{I}_v\rangle = Z_v^{-\frac{1}{2}} e^{-\frac{1}{2}\sum_l \omega_l a_l^\dagger a_l} |\boldsymbol{I}_v\rangle. \tag{11}$$

With the above definitions, the thermal Boltzmann distribution of Eq. (7) can be rewritten in the form

$$\rho_v = \mathrm{Tr}_{\tilde{\boldsymbol{k}}}\{|\mathbf{0}_v(\beta)\rangle\langle\mathbf{0}_v(\beta)|\} \tag{12}$$

where $\mathrm{Tr}_{\tilde{\boldsymbol{k}}}\{...\}$ indicates the trace over the tilde subspace. The equivalence of Eqs. (7) and (12) follows immediately from the orthogonality of the harmonic oscillator eigenvectors.

Let us now consider the Liouville – von Neumann equation identical to that of Eq. (1),

$$\partial_t \sigma(t) = -i[H + H_F(t), \sigma(t)], \tag{13}$$

but with the initial condition

$$\sigma(t_{in}) = |g\rangle\langle g||\mathbf{0}_v(\beta)\rangle\langle\mathbf{0}_v(\beta)|. \tag{14}$$

Then Eq. (12) guarantees that

$$\rho(t) = \mathrm{Tr}_{\tilde{\boldsymbol{k}}}\{\sigma(t)\}. \tag{15}$$

Furthermore, the Liouville - von Neumann equation

$$\partial_t \sigma(t) = -i[H + H_F(t) - \tilde{h}_v, \sigma(t)] \tag{16}$$

($\tilde{h}_v$ being any operator acting in the tilde subspace only) with the initial condition (14) fulfills Eq. (15).

Since the initial condition (14) corresponds to a pure state, the solution of Eq. (16) has the

$$\sigma(t) = |\psi(t)\rangle\langle\psi(t)| \tag{17}$$

where the wave function $|\psi(t)\rangle$ obeys the TFD Schrodinger equation

$$\partial_t |\psi(t)\rangle = -iH(t)|\psi(t)\rangle \tag{18}$$

with the initial condition

$$|\psi(t_{in})\rangle = |g\rangle|\mathbf{0}_v(\beta)\rangle. \tag{19}$$

For brevity, we have defined

$$H(t) = H + H_F(t) - \tilde{h}_v. \tag{20}$$

We have thus demonstrated that the solution of the original Liouville - von Neumann equation (1) with the initial condition (6) is equivalent to the solution of the TFD Schrodinger equation (18) with the initial condition (19).

The key advantage of the TFD representation is a compact analytical representation of the thermal vacuum state given by thermal Bogoliubov transformation

$$e^{-iG}|\mathbf{0}_v\tilde{\mathbf{0}}_v\rangle = |\mathbf{0}_v(\beta)\rangle \tag{21}$$

where $|\mathbf{0}_v\tilde{\mathbf{0}}_v\rangle$ is the ground state in the $|\boldsymbol{k}\rangle \otimes |\tilde{\boldsymbol{k}}\rangle$ subspace. Applying thermal Bogoliubov transformation to Eq. (18), we obtain

$$i\partial_t \big|\psi_\theta(t)\big\rangle = H_\theta(t)\big|\psi_\theta(t)\big\rangle \tag{22}$$

where

$$H_\theta(t) = e^{iG}H(t)e^{-iG}, \tag{23}$$

$$\big|\psi_\theta(t)\big\rangle = e^{iG}\big|\psi(t)\big\rangle \tag{24}$$

and

$$\big|\psi_\theta(t_{in})\big\rangle = |g\rangle|\mathbf{0}_v\tilde{\mathbf{0}}_v\rangle \tag{25}$$

is the global vacuum state. The nonlinear polarization of Eq. (8) can now be evaluated as

$$\mathcal{P}(t) = \big\langle\psi_\theta(t)\big|\hat{\mu}_\theta\big|\psi_\theta(t)\big\rangle \quad \text{with} \quad \hat{\mu}_\theta = e^{iG}\hat{\mu}e^{-iG}. \tag{26}$$

For thermal vacuum state $|\mathbf{0}_v(\beta)\rangle$ of Eq. (11), the operator of thermal Bogoliubov transformation reads [45–49]

$$G = -i\sum_j \theta_j(a_j\tilde{a}_j - a_j^\dagger\tilde{a}_j^\dagger) \tag{27}$$

where

$$\theta_j = \text{arctanh}(e^{-\beta\omega_j/2}). \tag{28}$$

For obtaining the explicit form of the transformed Hamiltonian $\bar{H}_\theta(t)$, we assume that electronic energies ε_n, electronic inter-state couplings J_{nm}, electron-vibrational intrastate couplings g_{nk}, and transition dipole moment vectors $\boldsymbol{\mu}_n$ are independent of vibrational coordinates. These approximations are commonly employed in molecular spectroscopy [1–7] and will be adopted in the present work. With these approximations, $\hat{\mu}_\theta = \hat{\mu}$. Then, by choosing

$$\tilde{h}_v(t) = \sum_k \omega_k\tilde{a}_k^\dagger\tilde{a}_k$$

we obtain the driven TFD Schrodinger equation

$$i\partial_t\big|\psi_\theta(t)\big\rangle = \left(H_\theta + H_F(t)\right)\big|\psi_\theta(t)\big\rangle \tag{29}$$

where [42]

$$H_\theta = e^{iG}He^{-iG} = \tag{30}$$

$$\sum_n \varepsilon_n c_n^\dagger c_n + \sum_{n\neq m} J_{nm}c_n^\dagger c_m + \sum_k \omega_k\left(a_k^\dagger a_k - \tilde{a}_k^\dagger\tilde{a}_k\right)$$

$$-\sum_{kn}\frac{g_{kn}}{\sqrt{2}}\left\{\left(a_k + a_k^\dagger\right)\cosh(\theta_k) + \left(\tilde{a}_k + \tilde{a}_k^\dagger\right)\sinh(\theta_k)\right\}c_n^\dagger c_n.$$

$H_F(t)$ depends on electronic degrees of freedom only and is unaffected by the TFD and Bogoliubov transformations. Eq. (29) solved with the initial condition (25) yields the nonlinear polarization

$$\mathcal{P}(t) = \big\langle \psi_\theta(t) \big| \hat{\mu} \big| \psi_\theta(t) \big\rangle. \tag{31}$$

The TFD Schrodinger equation (29) is governed by the TFD-LVC Hamiltonian H_θ of Eq. (30) and the system-field Hamiltonian $H_F(t)$ of Eq. (3). It is fully equivalent to the original Liouville – von Neumann equation (1). Hence the nonlinear polarizations of Eqs. (8) and (31) are identical. The number of vibrational modes in H_θ is double of that in the original Hamiltonian H of Eq. (2), and electron-vibrational couplings in H_θ are renormalized by temperature-dependent factors: $\cosh(\theta_k)$ for physical coordinates $x_k = \left(a_k + a_k^\dagger\right)/\sqrt{2}$ and $\sinh(\theta_k)$ for tilde coordinates $x_k = \left(\tilde{a}_k + \tilde{a}_k^\dagger\right)/\sqrt{2}$. If $T \to 0$ then $\theta_j \to 0$, the coupling to the tilde space disappears, and the standard Schrodinger equation is recovered as expected. Nonzero temperature causes dynamical mixing of the physical (a_k, $a_k^\dagger$) and tilde ($\tilde{a}_k$, $\tilde{a}_k^\dagger$) spaces. In actual simulations, we can drop those high-frequency tilde vibrational modes k for which the factors $\sinh(\theta_k)$ are smaller than a certain threshold. Such a flexibility of the TFD representation, which is absent in the traditional density matrix representation, decreases effective dimensionality of the problem and reduces computational burden.

It is important that only vibrational degrees of freedom are doubled in the TFD Schrodinger equation (29), while the number of the excitonic degrees of freedom remains unchanged. In a basis-set representation, the density matrix $\rho(t)$ in the Liouville – von Neumann equation (1) is an array of the dimension $(N_{ex} \times N_v)^2$, where N_{ex} (N_v) is the number of the basis functions specifying the excitonic and vibrational degrees of freedom. The wave function of the TFD Schrodinger equation, $\big|\psi_\theta(t)\big\rangle$, is an array of the dimension $N_{ex} \times N_v^2$. This yields a considerable reduction of dimension, notably for systems with multiple electronic states. For FMO, for example, $N_{ex} = 7$ and computational savings are substantial.

In the derivation of Eqs. (29) and (30), we assumed that the site energies ε_n, electronic couplings J_{nm} and electron-vibrational couplings g_{nk} in the original LVC Hamiltonian H of Eq. (2) as well as transition dipole moment vectors $\boldsymbol{\mu}_n$ in the system-field interaction Hamiltonian $H_F(t)$ of Eq. (3) were all constant. In many applications, however, these parameters are polynomial in vibrational creation-annihilation operators. For example, a

conical intersection between the states n and m driven by the vibrational coupling mode j corresponds to $J_{nm} \sim a_j + a_j^\dagger$ and transition dipole moments may depend on vibrational coordinates, $\boldsymbol{\mu}_n = \boldsymbol{\mu}_n^{(0)} + \sum_j (a_j + a_j^\dagger)\boldsymbol{\mu}_{nj}^{(1)}$ (non-Condon effects) [4]. In all these cases, the TFD Schrodinger equation with the TFD-LVC Hamiltonian can readily be constructed by using the fundamental relations [73]

$$e^{iG} a_j e^{-iG} = a_j \cosh(\theta_j) + \tilde{a}_j^\dagger \sinh(\theta_j), \tag{32}$$

$$e^{iG} \tilde{a}_j e^{-iG} = \tilde{a}_j \cosh(\theta_j) + a_j^\dagger \sinh(\theta_j). \tag{33}$$

III. THIRD-ORDER RESPONSE FUNCTIONS

From the formal point of view, the TFD Schrodinger equation (29) can be treated as the usual Schrodinger equation. Hence, all formal derivations, in particular perturbation theory in system-field interactions and the corresponding response functions will retain their form. The fundamental quantity describing the third-order response of the system on the external fields is the four-time correlation function of the transition dipole moment operators [1]. In our case, it explicitly reads

$$\Phi(\tau_4, \tau_3, \tau_2, \tau_1) = \langle \hat{\mu}(\tau_4)\hat{\mu}(\tau_3)\hat{\mu}(\tau_2)\hat{\mu}(\tau_1) \rangle \tag{34}$$

where the Heisenberg operators

$$\hat{\mu}(\tau) = e^{iH_\theta \tau} \hat{\mu} e^{-iH_\theta \tau} \tag{35}$$

are governed by the TFD Hamiltonian $\bar{H}_\theta$. The angular brackets in Eq. (34) mean

$$\langle ... \rangle \equiv \langle g | \langle \mathbf{0}_v \tilde{\mathbf{0}}_v | ... | \mathbf{0}_v \tilde{\mathbf{0}}_v \rangle | g \rangle. \tag{36}$$

Following Refs. [26, 74, 75], the fundamental correlation function Φ can be expressed as a sum of two contributions Φ^{s} and Φ^{d}, which correspond to the two situations in which, during the evolution from τ_2 to τ_3, the system is electronically in the ground state and in the double-exciton excited states, respectively (in both cases from τ_1 to τ_2 and from τ_3 to τ_4 the system is in single-exciton state):

$$\Phi(\tau_4, \tau_3, \tau_2, \tau_1) = \Phi^s(\tau_4, \tau_3, \tau_2, \tau_1) + \Phi^d(\tau_4, \tau_3, \tau_2, \tau_1). \tag{37}$$

Explicitly,

$$\Phi^s(\tau_4,\tau_3,\tau_2,\tau_1) = \langle\hat{\mu}_-(\tau_4)\hat{\mu}_+(\tau_3)\hat{\mu}_-(\tau_2)\hat{\mu}_+(\tau_1)\rangle \tag{38}$$

and

$$\Phi^d(\tau_4,\tau_3,\tau_2,\tau_1) = \langle\hat{\mu}_-(\tau_4)\hat{\mu}_-(\tau_3)\hat{\mu}_+(\tau_2)\hat{\mu}_+(\tau_1)\rangle\,. \tag{39}$$

$\Phi^{\rm s}$ describes the ground-state bleach (GSB) and stimulated-emission (SE) contributions to third-order spectroscopic signals, $\Phi^{\rm d}$ is responsible for excited-state absorption (ESA) and double-coherence signals.

The four-time correlation functions Φ^α ($\alpha = s,\, d$) generate 4 third-order response functions [26, 74, 75]:

$$R_1^\alpha(t_3,t_2,t_1) = \Phi^\alpha(t_1, t_1+t_2, t_1+t_2+t_3, 0), \tag{40}$$

$$R_2^\alpha(t_3,t_2,t_1) = \Phi^\alpha(0, t_1+t_2, t_1+t_2+t_3, t_1), \tag{41}$$

$$R_3^\alpha(t_3,t_2,t_1) = \Phi^\alpha(0, t_1, t_1+t_2+t_3, t_1+t_2), \tag{42}$$

$$R_4^\alpha(t_3,t_2,t_1) = \Phi^\alpha(t_1+t_2+t_3, t_1+t_2, t_1, 0). \tag{43}$$

With these definitions, nonlinear optically-induced third-order polarization can be evaluated as

$$\mathcal{P}(t) = \int_0^\infty dt_1 \int_0^\infty dt_2 \int_0^\infty dt_3\; S(t_1,t_2,t_3)E(t-t_3)E(t-t_3-t_2)E(t-t_3-t_2-t_1) \tag{44}$$

where

$$S(t_1,t_2,t_3) = -i\sum_{k=1}^{4}\sum_{\alpha=s,d}\{R_k^\alpha(t_3,t_2,t_1) - [R_k^\alpha(t_3,t_2,t_1)]^*\}. \tag{45}$$

In terms of the TFD Hamiltonian H_θ of Eq. (30), the four-time response functions (38) and (39) read:

$$\Phi^s(\tau_4,\tau_3,\tau_2,\tau_1) = \langle g|\langle\mathbf{0}_v\tilde{\mathbf{0}}_v|\hat{\mu}_- e^{-iH_\theta(\tau_4-\tau_3)}\hat{\mu}_+ e^{-iH_\theta^v(\tau_3-\tau_2)}\hat{\mu}_- e^{-iH_\theta(\tau_2-\tau_1)}\hat{\mu}_+|\mathbf{0}_v\tilde{\mathbf{0}}_v\rangle|g\rangle, \tag{46}$$

$$\Phi^d(\tau_4,\tau_3,\tau_2,\tau_1) = \langle g|\langle\mathbf{0}_v\tilde{\mathbf{0}}_v|\hat{\mu}_- e^{-iH_\theta(\tau_4-\tau_3)}\hat{\mu}_- e^{-iH_\theta(\tau_3-\tau_2)}\hat{\mu}_+ e^{-iH_\theta(\tau_2-\tau_1)}\hat{\mu}_+|\mathbf{0}_v\tilde{\mathbf{0}}_v\rangle|g\rangle. \tag{47}$$

In writing the above expressions, we employ the conservation of the number of excitons, deriving from the commutation property

$$[H_\theta,\hat{N}] = 0,\;\; \hat{N} \equiv \sum_{k=1} c_k^\dagger c_k, \tag{48}$$

and set the zero-point energy of the vibrational ground state, $E_{\mathbf{0}}$, to zero

$$H_\theta|\mathbf{0}_v\tilde{\mathbf{0}}_v\rangle|g\rangle = E_{\mathbf{0}}|\mathbf{0}_v\tilde{\mathbf{0}}_v\rangle|g\rangle = 0. \tag{49}$$

If necessary, $E_{\mathbf{0}}$ can be readily reintroduced in the final formulas. In addition, $\exp\{-iH_\theta(\tau_3-\tau_2)\}$ in Eq. (46) is replaced by $\exp\{-iH_\theta^v(\tau_3-\tau_2)\}$ where

$$H_\theta^v = \sum_k \omega_k \left(a_k^\dagger a_k - \tilde{a}_k^\dagger \tilde{a}_k\right), \tag{50}$$

because during the time interval $\tau_3 - \tau_2$ the system evolves in its ground excitonic state.

To make Eq. (46) more explicit, and easier to implement in our TFD-TT approach we proceed as follows. First, we define single-exciton states

$$|e_n\rangle = c_n^\dagger|g\rangle. \tag{51}$$

Then the TFD Hamiltonian in the singly-excited state manifolds reads

$$H_\theta^{(s)} = \sum_n \varepsilon_n|e_n\rangle\langle e_n| + \sum_{n\neq m} J_{nm}|e_n\rangle\langle e_m| + \sum_k \omega_k \left(a_k^\dagger a_k - \tilde{a}_k^\dagger \tilde{a}_k\right)$$

$$-\sum_{kn}\frac{g_{kn}}{\sqrt{2}}\left\{\left(a_k + a_k^\dagger\right)\cosh(\theta_k) + \left(\tilde{a}_k + \tilde{a}_k^\dagger\right)\sinh(\theta_k)\right\}|e_n\rangle\langle e_n|$$

and the transition dipole moment operators assume the form

$$\hat{\mu}_- = |g\rangle\langle e|, \;\; \hat{\mu}_+ = |e\rangle\langle g| \tag{52}$$

where

$$|e\rangle = \sum_n (\boldsymbol{s}\boldsymbol{\mu}_n)|e_n\rangle. \tag{53}$$

It is also convenient to define the TFD wavefunction

$$|\psi(\tau)\rangle = e^{-iH_\theta\tau}\hat{\mu}_+|\mathbf{0}_v\tilde{\mathbf{0}}_v\rangle|g\rangle = e^{-iH_\theta^{(s)}\tau}|\mathbf{0}_v\tilde{\mathbf{0}}_v\rangle|e\rangle, \tag{54}$$

the vibrational propagator

$$U(\tau) = e^{-iH_\theta^v\tau} \tag{55}$$

and the excitonic operator

$$B = \hat{\mu}_+\hat{\mu}_- = |e\rangle\langle e|. \tag{56}$$

With this notation,

$$\Phi^s(\tau_4,\tau_3,\tau_2,\tau_1) = \langle\psi(\tau_3-\tau_4)|BU(\tau_3-\tau_2)|\psi(\tau_2-\tau_1)\rangle. \tag{57}$$

This is one of the key theoretical results of the present work.

Plugging the definitions (40)-(43) into Eq. (A7) one obtains explicit expressions for the single-exciton response functions:

$$R_1^s(t_3,t_2,t_1) = \langle\psi(t_2)|BU^\dagger(t_3)|\psi(t_1+t_2+t_3)\rangle, \tag{58}$$

$$R_2^s(t_3,t_2,t_1) = \langle\psi(t_1+t_2)|BU^\dagger(t_3)|\psi(t_2+t_3)\rangle,$$

$$R_3^s(t_3,t_2,t_1) = \langle\psi(t_1)|BU^\dagger(t_2+t_3)|\psi(t_3)\rangle,$$

$$R_4^s(t_3,t_2,t_1) = \langle\psi(t_3)|^*BU(t_2)|\psi(t_1)\rangle$$

($*$ denotes complex conjugation). In the above formulas, R_1 and R_2 describe evolution of the system in the single-exciton manifold during t_2 and are responsible for the SE contribution. R_3 and R_4 describe evolution of the system in the ground excitonic state during t_2 and are responsible for the GSB contribution.

We note that the evaluation of these response functions requires computation of just a *single* TFD-TT wavefunction $|\psi(\tau)\rangle$. Evaluation of Φ^d is much more involved and considered in Appendix B.

Due to isotropy of space, the system as a whole does not have a preferential orientation. Hence Φ^α and R_k^α should be averaged over orientations of transition dipole moment vectors $\boldsymbol{\mu}_n$. The details of this procedure and the explicit expressions for $\bar{\Phi}^\alpha$ and $\bar{R}_k^\alpha$ (the averaging is denoted by overbar) are given in Appendix C. With the efficient averaging procedure developed in [76], $\bar{\Phi}^\alpha$ and $\bar{R}_k^\alpha$ can be computed by the evaluation of just *three* TFD-TT wavefunctions $|\psi_a(\tau)\rangle$ defined per Eq. (C7), $a = x, y, z$.

IV. EVALUATION OF RESPONSE FUNCTIONS IN THE TT REPRESENTATION

As already noted, the basic ingredient for evaluation of the single-exciton response function Φ^s is a single real time propagation of the initial vacuum state. To show how the procedure works in the TT representation, we consider the response function $R_1^s(t_3, t_2, t_1)$ of Eq. (A8) and rewrite it in the form

$$R_1^s(t_3, t_2, t_1) = \langle \psi(t_2) | B U^\dagger(t_3) | \psi(t_1 + t_2 + t_3) \rangle \tag{59}$$

where the wavefunction $|\psi(t_2)\rangle$ is determined by Eq. (A4), the operator B defined by Eq. (A6) operates exclusively in the excitonic subspace, and $U(t)$ defined by Eq. (A5) is the vibrational propagator in the electronic ground state (see the Appendix A for the explicit formulae and other details). Since H_θ^v of Eq. (50) is separable into $2N_v$ non-interacting terms this latter operator is nothing but the direct product of $2N_v$ diagonal exponential operators

$$U(t) = \prod_{k=1}^{2N_v} U_k(t) = \prod_{k=1}^{2N_v} e^{-i\omega_k n_k t} \tag{60}$$

where n_k is the occupation number operator of the k-th vibrational mode in the physical or tilde space.

In our approach the TFD Schrödinger equation is solved using the TT representation, in combination with a time-dependent variational integration scheme [41–44]. A variety of applications have shown that this method is very robust and well suited for many-dimensional electron-vibrational problems [41–44, 50–52]. The TT representation of $|\psi(t)\rangle$ is written as

$$|\psi(t)\rangle = \sum_{i_1, i_2, \ldots i_N} A_1(i_1; t) A_2(i_2; t) \ldots A_N(i_N; t) |i_1, i_2 \ldots i_N\rangle \tag{61}$$

where $|i_1, i_2 \ldots i_N\rangle$ labels the basis state, $N = 2N_v + 1$, and the $A_k(i_k; t)$, $k = 1, \ldots N$ are time-dependent complex rectangular matrices of sizes $r_{k-1} \times r_k$ called *core* of the tensor. The indices r_k are the ranks of the TT and, since each term in the product is a complex scalar, the boundary condition $r_0 = r_N = 1$ must be fulfilled. In our specific case the index i_1 labels the excitonic states and the remaining $2N_v$ indices label the physical and tilde vibrational degrees of freedom.

We now notice that the operators B and U_k of Eq. (59) act on different variables, and hence on different indices of the state vector $|\psi(t_2)\rangle$. Using well known properties of TTs

[50–52] we can easily compute the cores $C_k(i_k;t)$ of the TT representation of the vector $|\phi(t_2,t_3)\rangle = BU(t_3)|\psi(t_2)\rangle$ as

$$C_1(i_1;t_2) = \sum_{j_1,\ldots,j_N} B(i_1,j_1)A_1(j_1;t_2) \tag{62}$$

$$C_k(i_k;t_2,t_3) = \sum_{j_1,\ldots,j_N} U_k(i_k,j_k;t_3)A_k(j_k;t_2) \qquad k = 2,...,2N_v+1 \tag{63}$$

where $B(i_1,j_1)$ and $U_k(i_k,j_k;t)$ are the matrix representations of the operators B and U_k. $R_1^s(t_3,t_2,t_1)$ is given then by the scalar product $\langle\phi(t_2,t_3)|\psi(t_1+t_2+t_3)\rangle$ which can be computed with efficient TT algorithms [50].

V. TIME- AND FREQUENCY-RESOLVED EMISSION OF FMO

For the explicit evaluation of R_k^s, we adopt the FMO model which is equivalent to Model II of Ref. [77]. It describes 7 identical bacteriochlorophyll molecules (BChls), each of which is modeled as an electronic two-state system possessing two vibrational modes with frequencies $\omega_1 = 200$ cm^{-1} ($2\pi/\omega_1 = 167$ fs) and $\omega_2 = 160$ cm^{-1} ($2\pi/\omega_2 = 208$ fs). These modes have been recently detected experimentally [64, 68] and are very close to those appearing from single molecule spectroscopic data [**?**]. Since $\beta^{-1} = 0.026$ eV =210 cm^{-1} at $T = 300$ K, temperature effects are important for both modes. The electron-vibrational couplings are $\kappa_1 = 0.289$ and $\kappa_2 = 0.175$. The values of ε_k and $J_{kk'}$ are taken from Ref. [42, 78]. The transition dipole moment vectors of the BChls were assumed to be along the two nitrogen atoms $N_B - N_D$ [79], and positions of these atoms were we retrieved from the protein data bank [80, 81]. The response functions $R_k^s(t_3,t_2,t_1)$ were computed on the three-dimensional grid: 75 points along t_3 with time step 10 fs, 150 points along t_2 with time step 5 fs, 20 points along t_1 with time step 1 fs. Orientational averaging was performed as explained in Appendix C. Static disorder in ε_k is assumed to be Gaussian with variance $\sigma = 100$ cm^{-1}. The response functions $\bar{R}_k^s(t_3,t_2,t_1)$ were evaluated upon averaging over $\mathcal{N} = 100$ random realizations of static disorder, which was enough for obtaining converged results (see below).

Omitting a frequency-depending prefactor which is irrelevant for the present discussion, we can express the time- and frequency-resolved fluorescence signals in terms of response functions as follows [82, 83]:

$$I(t,\omega) \sim \mathrm{Re}\int_{-\infty}^{\infty} dt' \int_0^{\infty} dt_3 \int_0^{\infty} dt_2 \int_0^{\infty} dt_1 \times \tag{64}$$

$$\mathcal{E}_g(t'-t)\mathcal{E}_g(t'-t_3-t)\mathcal{E}_p(t-t_3-t_2)\mathcal{E}_p(t-t_3-t_2-t_1)\times$$

$$e^{-(\gamma-i\omega)t_3}\left\{R_1^s(t_3,t_2,t_1)e^{i\omega_p t_1}+R_2^s(t_3,t_2,t_1)e^{-i\omega_p t_1}\right\}.$$

Here t is the time delay between the pump pulse and the up-conversion (gate) pulse, ω is the detected fluorescence frequency, ω_p and $\mathcal{E}_p(t)$ are the carrier frequency and the dimensionless envelope of the pump pulse, $\mathcal{E}_g(t)$ is the dimensionless envelope determining the temporal resolution of the gate, and the parameter $0 \leq \gamma < \infty$ controls the spectral resolution of the gate: $\gamma = 0$ corresponds to perfect spectral resolution, while $\gamma \to \infty$ yields poor time resolution [84].

Physically, the time- and frequency-resolved fluorescence spectrum is defined as the rate of emission of photons of frequency ω at time t. Qualitatively, $I(t,\omega)$ can be interpreted as the projection of the wave packet in the excited excitonic state(s) onto the vibrational states of the excitonic ground state. If the pump pulse can be assumed instantaneous, while the gate pulse is short on the system dynamics timescale, but long on the electronic dephasing timescale and $\gamma = 0$ (perfect time and frequency resolution), then we obtain the so-called ideal fluorescence signal

$$I_{id}(t,\omega) \sim \mathrm{Re}\int_0^\infty dt_3 e^{i\omega t_3}R_1^s(t_3,t,0). \tag{65}$$

$I_{id}(t,\omega)$ cannot be detected in a fluorecence up-conversion experiment, because the frequency and time resolution of the signal are determined by the duration of the gate pulse and are Fourier-limited [85, 86]. Nowadays ~ 10 fs pump pulses are common in spectroscopic labs, while ~ 50 fs resolution is currently achievable in fluorescence up-conversion [9, 87]. In our simulations, the pump pulse was modeled by a Gaussian, $\mathcal{E}_p(t) = \exp\{-(t/\tau_p)^2\}$, and $\tau_p = 15$ was fixed. For the present FMO model, excitation with this pulse is indistinguishable from impulsive (instantaneous) excitation. The gate pulse was also assumed to be Gaussian, $\mathcal{E}_g(t) = \exp\{-(t/\tau_g)^2\}$, but its duration τ_g was varied to explore how a finite gate time affects $I(t,\omega)$. Spectral resolution was assumed perfect ($\gamma = 0$). To give shape to spectral features of ideal signals, $I_{id}(t,\omega)$ were calculated with electronic dephasing time $\tau_d = 200$ fs ($R_k^s(t_3,t_2,t_1) \to R_k^s(t_3,t_2,t_1)\exp\{-(t_3+t_1)/\tau_d\}$). All real signals $I(t,\omega)$ were calculated without phenomenological dephasing parameters ($\tau_d^{-1} = 0$): As follows from Eq. (64) and

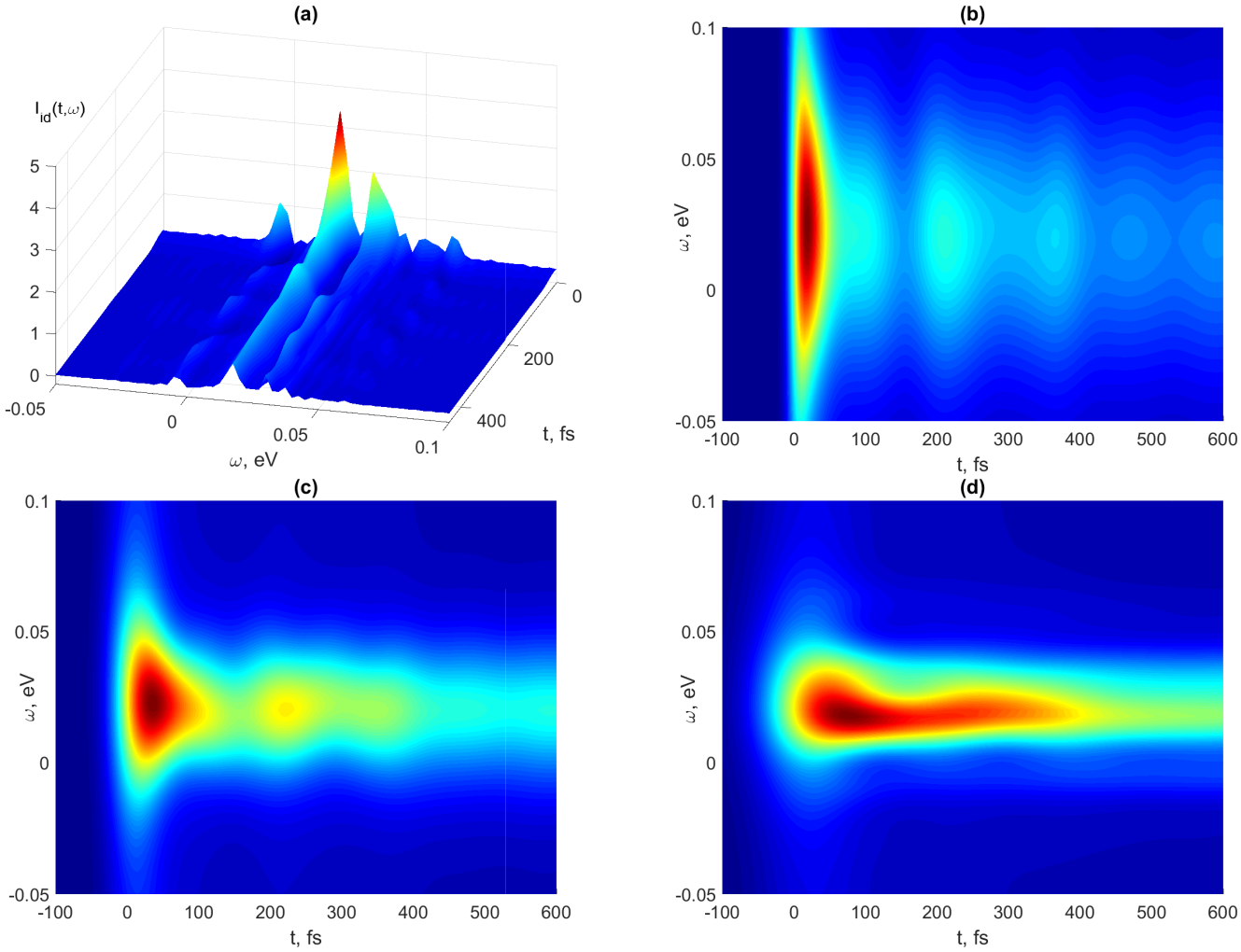

Figure 1: Time- and frequency-resolved fluorescence spectra $I(t,\omega)$ of FMO without static disorder: (a) ideal, (b) $\tau_g = 20$ fs, (c) $\tau_g = 50$ fs, (d) $\tau_g = 100$ fs. For better visualization, top view of $I(t,\omega)$ is presented in panels (b)-(d).

is confirmed by explicit calculations, spectral resolution of $I(t,\omega)$ is controlled by the gate pulse duration for $\tau_d > \tau_g$. In all time- and frequency-resolved spectra considered below, the origin of the frequency axis is set at the excitonic energy of BChl #3.

Fig. 1 shows time- and frequency-resolved fluorescence spectra of FMO calculated without averaging over static disorder. Ideal signal $I_{id}(t,\omega)$ is depicted in panel (a). As typical for ideal fluorescence spectra [85, 86], it combines time resolution (oscillatory transients in the time domain) and frequency resolution (peaks in the frequency domain). We note that the spectral features do not reveal purely excitonic nor vibrational frequencies. The peaks are of vibronic character caused by strong exciton-vibrational coupling: despite relatively

small coupling constants κ_a and, correspondingly, small Huang-Rhys factors $\kappa_a^2/2$, ω_a match quite well excitonic energy difference ($a = 1, 2$) (see the discussion in Refs. [88–93]). The spectrum $I_{id}(t, \omega)$ shows pronounced oscillations along t at a given ω, which are of vibronic origin (*vide infra*).

Panels (b)-(d) of Fig. 1 show time- and frequency-resolved fluorescence spectra $I(t, \omega)$ calculated with decreasing time resolution, from good ($\tau_g = 20$ fs, panel (b)) through intermediate ($\tau_g = 50$ fs, panel (c)) to poor ($\tau_g = 100$ fs, panel (d)). Clearly, the spectral resolution of $I(t, \omega)$ increases and the spectral width shrinks with τ_g. In addition, the spectral width of $I(t, \omega)$ shrinks with t for fixed τ_g due to dephasing of vibronic modes contributing to the wavepacket motion. The signals in panels (b) and (c) exhibit pronounced wavepacket dynamics. The wavepacket motion is almost symmetric relative to the line $\omega = 0.025$ eV, which is caused my small Huang-Rhys factors of BChls and therefore small κ_a of the present FMO model. $I(t, \omega)$ in panels (b) and (c) exhibit pronounced revivals of vibronic origin (notably the one around $t = 230$ fs) which are readily detectable when the gate pulse is short enough (cf. Refs. [88–91]). For $\tau_g = 100$ fs (panel (d)), duration of the gate pulse is comparable with the characteristic times vibronic oscillations. Hence the latter are smeared out, and the time resolution of $I(t, \omega)$ is almost lost in 1(d).

To obtain a more detailed view of the wavepacket dynamics, Fig. 2 shows the time evolution of cuts of $I(t, \omega)$ at specific ω covering the most significant spectral width, from -0.0075 to 0.0425 eV. The cuts in all panels exhibit pronounced but quite irregular oscillations of vibronic origin, the detection of which depends crucially on temporal resolution of gating. The cuts of $I_{id}(t, \omega)$ in panel (a) are all quite erratic. The cuts of $I(t, \omega)$ in panel (b), which corresponds to a good time resolution, are all similar and exhibit pronounced oscillations of vibronic origin. However, these oscillations cannot be pinned down to several fundamental harmonic frequencies. For $\tau_g = 50$ fs (panel (b)), short-period wiggles are smoothed out, while the remaining larger amplitude and longer-period structures remain. If temporal resolution further decreases ($\tau_g = 100$ fs, panel (d)) the time resolution is almost lost and the oscillatory features merge into rather irregular but still non-monotonic evolutions.

We now examine the effect of static disorder on $I(t, \omega)$. Fig. 3 shows a cut of the fluorescence spectrum $I(t, \omega)$ at $\omega = 0.03$ eV for good time resolution ($\tau_g = 20$ fs) evaluated for increasing number $\mathcal{N}$ of random realizations of static disorder. It is evident that static disorder has a significant impact on $I(t, \omega)$ (the details of behavior of the signals are discussed

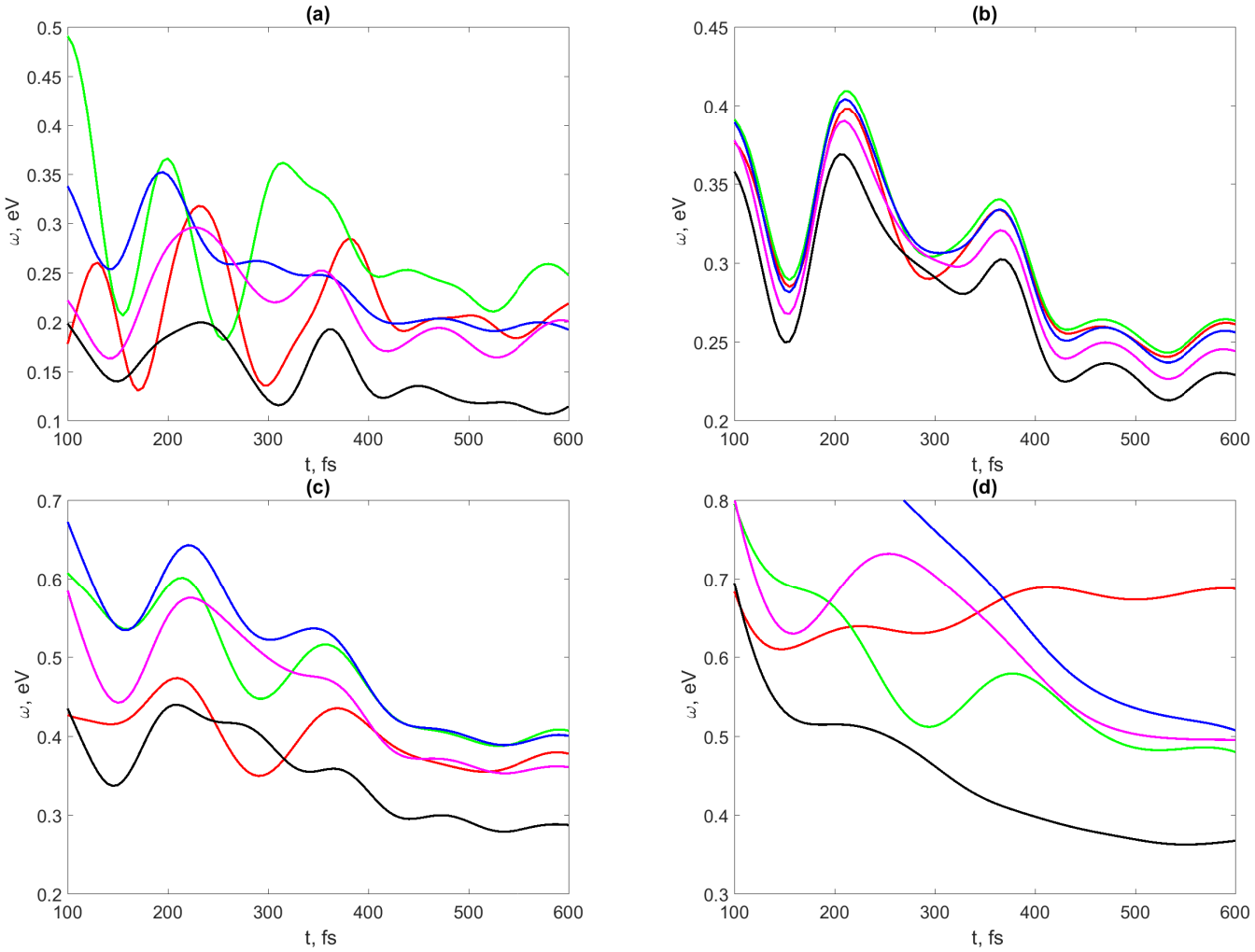

Figure 2: Cuts of time- and frequency-resolved fluorescence spectra $I(t,\omega)$ of FMO at $\omega = -0.0075$ eV (red), $\omega = 0.005$ eV (green), $\omega = 0.0175$ eV (blue), $\omega = 0.03$ eV (magenta) and $\omega = 0.0425$ eV (black) calculated without static disorder: (a) ideal, (b) $\tau_g = 20$ fs, (c) $\tau_g = 50$ fs, (d) $\tau_g = 100$ fs. The cuts are normalized to 1 at $t = 0$.

below), and that the signal evaluated with $\mathcal{N} = 100$ can be considered converged.

Fig. 4 shows time- and frequency-resolved fluorescence spectra of FMO obtained after averaging over static disorder. It is quite evident that the oscillatory features in the ideal signal $I_{id}(t,\omega)$ in panel (a) as well as in real signals in $I(t,\omega)$ in panels (b)-(d) are more regular and smoother in Fig. 4 than in Fig. 1. Furthermore, the shapes and locations of these oscillatory features change considerably, as is evident from the comparison of signals in panels (b) and (c) in Figs. 4 and 1.

A more detailed and quantitative explanation of the impact of static disorder on the fluorescence signals can be obtained from the analysis of Fig. 5, which shows cuts of $I(t,\omega)$

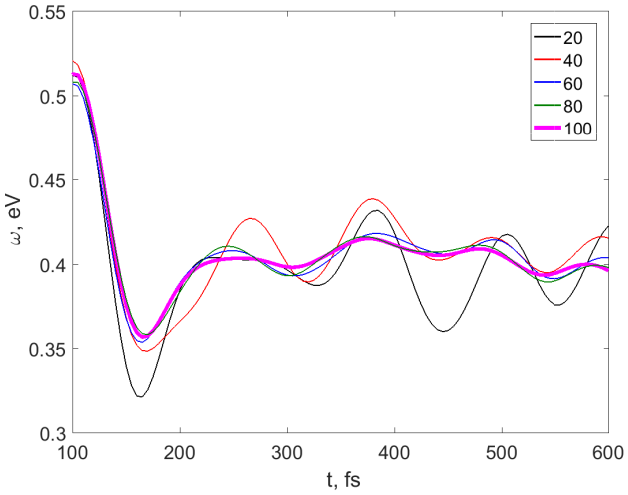

Figure 3: Cut of time- and frequency-resolved fluorescence spectra $I(t,\omega)$ of FMO at $\omega = 0.03$ eV and good time resolution ($\tau_g = 20$ fs) averaged over $\mathcal{N}$ realizations of static disorder indicated in the legend.

of Fig. 4 at specific ω. Indeed, the cuts in Fig. 5(a) corresponding to $I_{id}(t,\omega)$ are quite regular. The cuts in Fig. 5(b) for $t > 300$ fs exhibit oscillations with a period of ~ 100 fs which reveal 2nd overtone of the second vibrational mode, $2\pi/(2\omega_2) = 104$ fs. The features revealing 2nd overtone of ω_2 start to merge and produce different patterns in Fig. 5(c), because the gate time with $\tau_g = 50$ fs is just half of the period of 2nd overtone, which is insufficient for resolving the corresponding oscillatory motion. The cuts in Fig. 5(d) for $\tau_g = 100$ fs show non-monotonic evolutions which are difficult to analyze and impossible to associate with a specific vibrational frequency.

The signal $I(\omega,t)$ evaluated for a good time resolution (see 5(b))has two distinct features.

(i) 2nd overtones of vibrational modes frequently manifest themselves in spectroscopic signals [94, 95]. Indeed, the motion of an excited-state wavepacket modulates the signal intensity $I(t,\omega)$, thus if a maximum of the fluorescence intensity corresponds to the position of the wavepacket along the dominant Franck-Condon-active vibrational mode somewhere in between the turning points of its motion, the wavepacket will cross this positions twice per period.

(ii) As shown in Ref. [77], the expectation variable of any dynamical variable A averaged over static disorder with a characteristic dispersion σ exhibits predominantly vibrational oscillations at $t > 2\pi/\sigma$ and can be represented as

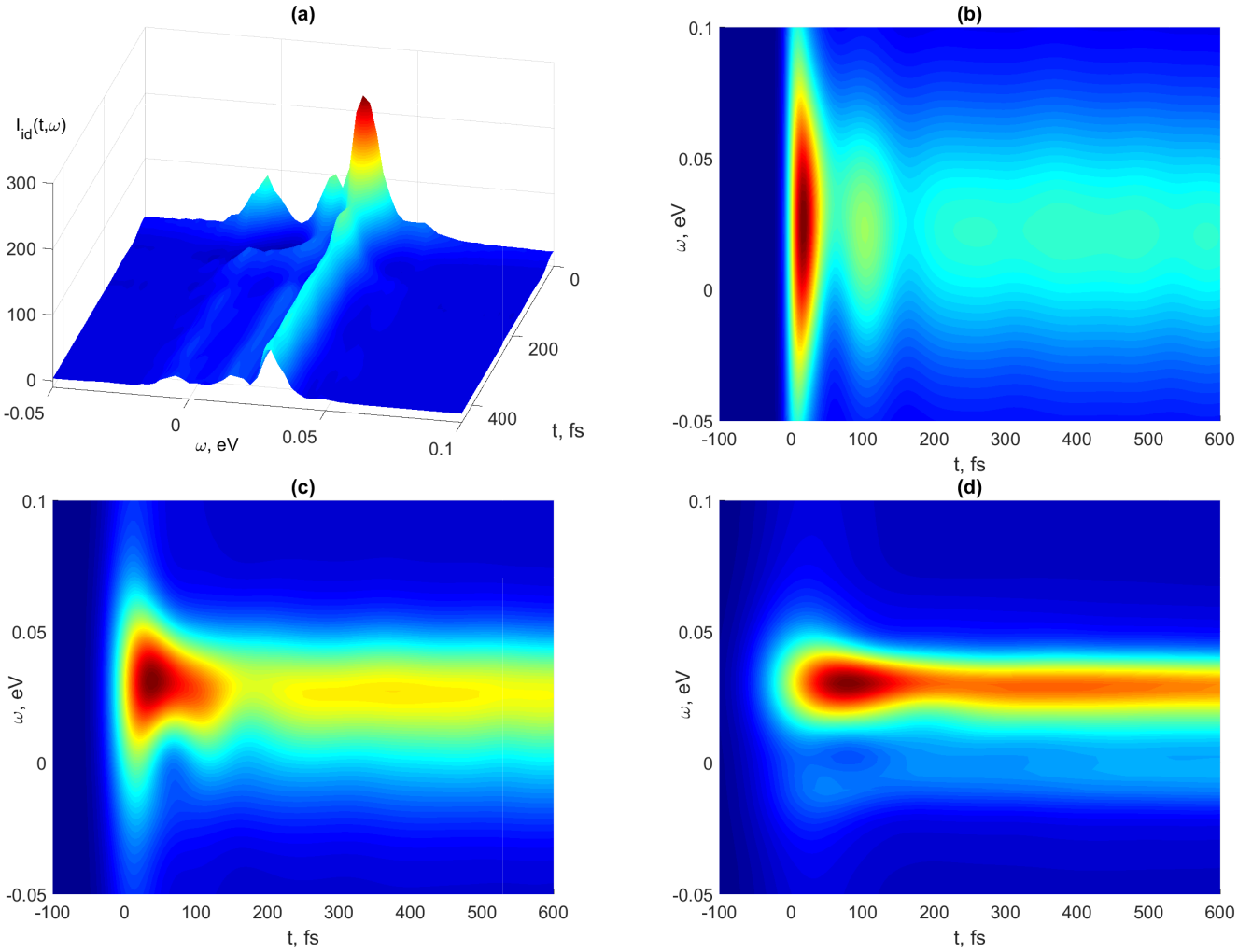

Figure 4: Time- and frequency-resolved fluorescence spectra $I(t,\omega)$ of FMO calculated after averaging over static disorder: (a) ideal, (b) $\tau_g = 20$ fs, (c) $\tau_g = 50$ fs, (d) $\tau_g = 100$ fs. For better visualization, top view of $I(t,\omega)$ is presented in panels (b)-(d).

$$\left\langle e^{iH_\theta t} A e^{-iH_\theta t} \right\rangle_\sigma \approx \sum_k \sum_{m=0}^{M_k} a_{km}(t) \cos(m\omega_k t - \varphi_{km}(t)). \tag{66}$$

Here $\langle ... \rangle_\sigma$ indicates the trace and averaging over static disorder, $a_{km}(t)$, $\varphi_{km}(t)$ are some slowly varying functions of time, and M_k is the maximal number of overtones for the kth vibrational mode. The excitonic populations averaged over static disorder, which were studied in Ref. [77] for the same FMO model, also exhibited vibrational oscillations featuring ω_2. The response functions, and notably spectroscopic signals, cannot be expressed in terms of the simple expression in the l.h.s. of Eq. (66). Nevertheless, the cuts of $I(t,\omega)$ in 5(b) unequivocally show that the behavior predicted by the r.h.s. of Eq. (66) can indeed be

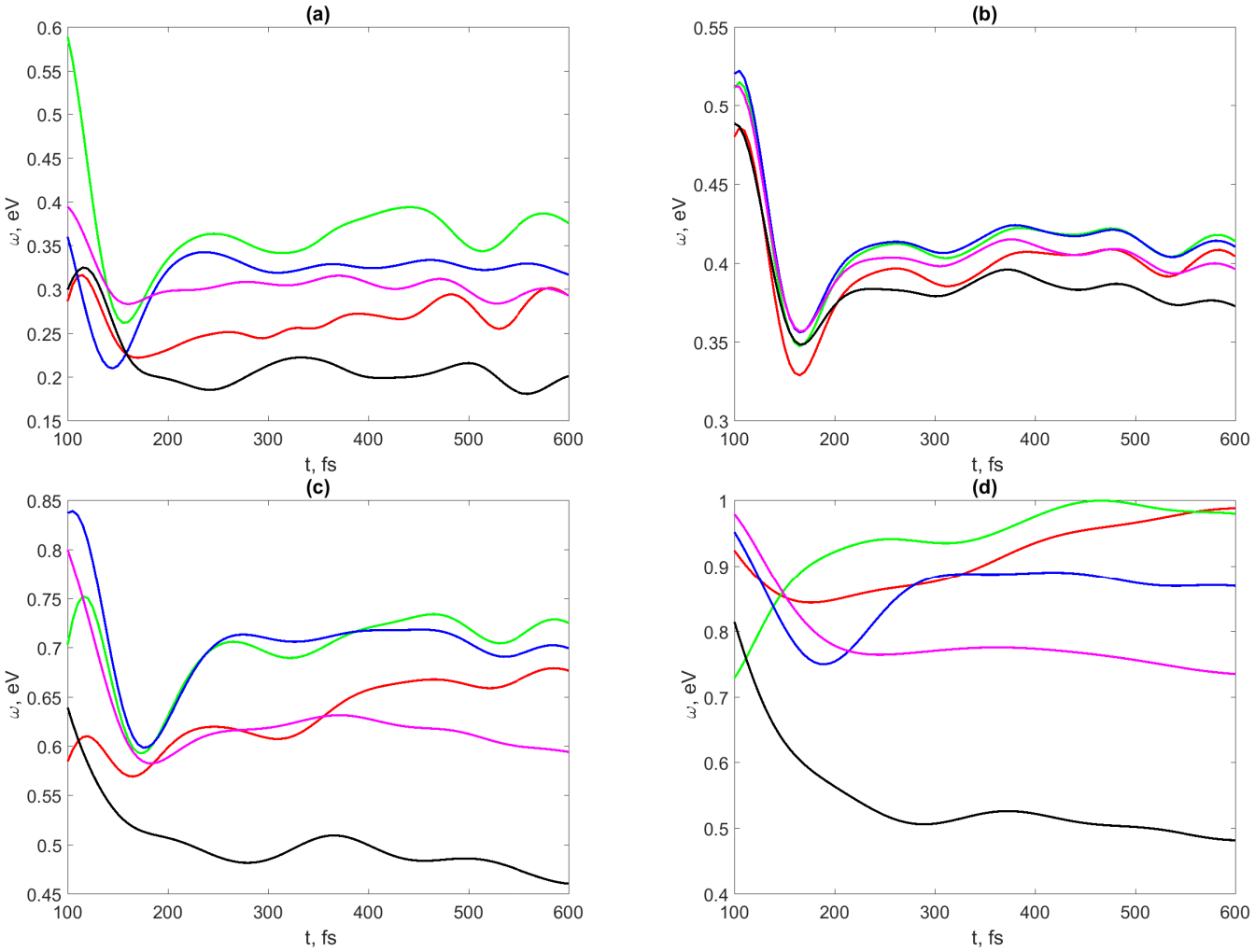

Figure 5: Cuts of time- and frequency-resolved fluorescence spectra $I(t,\omega)$ of FMO at $\omega = -0.0075$ eV (red), $\omega = 0.005$ eV (green), $\omega = 0.0175$ eV (blue), $\omega = 0.03$ eV (magenta) and $\omega = 0.0425$ eV (black) calculated after averaging over static disorder: (a) ideal, (b) $\tau_g = 20$ fs, (c) $\tau_g = 50$ fs, (d) $\tau_g = 100$ fs. The cuts are normalized to 1 at $t = 0$.

detected in time- and frequency-resolved fluorescence of FMO provided the time resolution of gating is sufficient. Hence purely vibrational beatings recently detected in femtosecond signals of FMO [64, 68] may be caused not only by the wavepacket motion in the excitonic ground state [90], but also by "melting" of vibronic frequencies into vibrational frequencies upon averaging over static disorder, as predicted by Eq. (66). Note that there exist other mechanisms of long-lived predominantly vibrational responses in the excited electronic states [97], and existence of disorder-induced purely excitonic oscillations has also been predicted [98].

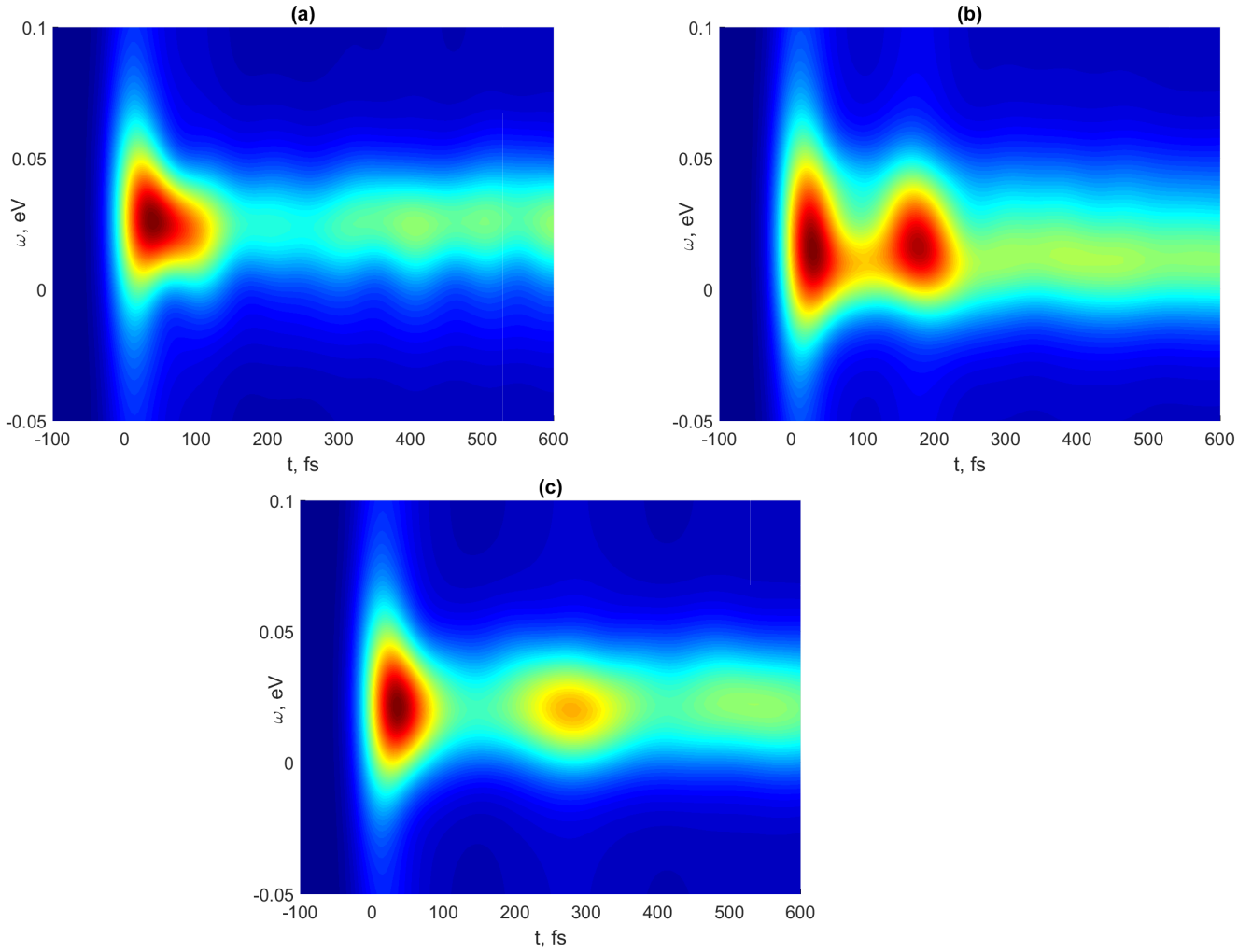

Figure 6: Top views of time- and frequency-resolved fluorescence spectra $I(t,\omega)$ of FMO for $\tau_g = 50$ fs calculated for three random realizations of ε_k and $J_{kk'}$ sampled from Gaussians with variance $\sigma = 100$ cm^{-1}.

To complete the discussion, $I(t,\omega)$ of FMO for $\tau_g = 50$ fs calculated for three random realizations of ε_k sampled from Gaussians with variance $\sigma = 100$ cm^{-1} are presented in 6. These random realizations mimic different FMO mutants experimentally studied in Ref. [64]. It is essential that all three signals are substantially different and exhibit vibronic revivals at different times. Yet, averaging of $I(t,\omega)$ over static disorder results in the signal in Fig. 4(c) which reveals qualitatively different spectral features.

VI. CONCLUSIONS

We have developed a methodology for numerically accurate fully quantum simulation of nonlinear electronic femtosecond signals of polyatomic molecules and molecular aggregates at finite temperature. The methodology is based on the Thermo Field Dynamics (TFD) representation of the driven quantum dynamics and tensor-train (TT) methods for efficient simulation of spectroscopic third-order response functions.

The methodology was applied to the simulation time- and frequency-resolved fluorescence signals of the Fenna–Matthews–Olson (FMO) complex. The signals show a pronounced wave-packet motion in the single-exciton states of FMO and depend strongly on the time resolution of the up-conversion process. In the time domain, the signals exhibit pronounced oscillations of vibronic origin provided static disorder in excitonic energies and couplings can be neglect. Upon averaging over static disorder with variance $\sigma = 100$ cm^{-1}, the signals exhibit predominantly vibrational oscillations caused by "melting" of vibronic frequencies into vibrational frequencies upon averaging over static disorder. If the time resolution is sufficient, such disorder-induced vibrational oscillations may become visible in various femtosecond signals.

Work is in progress on further generalization of our methodology towards description of open quantum systems along the lines developed in Refs. [96, 99, 100].

Appendix A: Explicit formulas for single-exciton response functions

To make Eq. (46) explicit, we define single-exciton states

$$|e_n\rangle = c_n^\dagger |g\rangle. \tag{A1}$$

Then the TFD Hamiltonian in the singly-excited state manifolds reads

$$H_\theta^{(s)} = \sum_n \varepsilon_n |e_n\rangle\langle e_n| + \sum_{n\neq m} J_{nm}|e_n\rangle\langle e_m| + \sum_k \omega_k \left(a_k^\dagger a_k - \tilde{a}_k^\dagger \tilde{a}_k\right)$$

$$- \sum_{kn} \frac{g_{kn}}{\sqrt{2}} \left\{ \left(a_k + a_k^\dagger\right)\cosh(\theta_k) + \left(\tilde{a}_k + \tilde{a}_k^\dagger\right)\sinh(\theta_k) \right\} |e_n\rangle\langle e_n|$$

and the transition dipole moment operators assume the form

$$\hat{\mu}_- = |g\rangle\langle e|, \;\; \hat{\mu}_+ = |e\rangle\langle g| \tag{A2}$$

where

$$|e\rangle = \sum_n (\boldsymbol{s}\boldsymbol{\mu}_n)|e_n\rangle. \tag{A3}$$

It is also convenient to define the TFD wavefunction

$$|\psi(\tau)\rangle = e^{-iH_\theta \tau}\hat{\mu}_+ |\mathbf{0}_v\tilde{\mathbf{0}}_v\rangle|g\rangle = e^{-iH_\theta^{(s)}\tau}|\mathbf{0}_v\tilde{\mathbf{0}}_v\rangle|e\rangle, \tag{A4}$$

the vibrational propagator

$$U(\tau) = e^{-iH_\theta^v \tau} \tag{A5}$$

and the excitonic operator

$$B = \hat{\mu}_+\hat{\mu}_- = |e\rangle\langle e|. \tag{A6}$$

With this notation,

$$\Phi^s(\tau_4,\tau_3,\tau_2,\tau_1) = \langle\psi(\tau_3-\tau_4)|BU(\tau_3-\tau_2)|\psi(\tau_2-\tau_1)\rangle. \tag{A7}$$

This is one of the key theoretical results of the present work.

Plugging the definitions (40)-(43) into Eq. (A7) one obtains explicit expressions for the single-exciton response functions:

$$R_1^s(t_3,t_2,t_1) = \langle\psi(t_2)|BU^\dagger(t_3)|\psi(t_1+t_2+t_3)\rangle, \tag{A8}$$

$$R_2^s(t_3,t_2,t_1) = \langle\psi(t_1+t_2)|BU^\dagger(t_3)|\psi(t_2+t_3)\rangle,$$

$$R_3^s(t_3,t_2,t_1) = \langle\psi(t_1)|BU^\dagger(t_2+t_3)|\psi(t_3)\rangle,$$

$$R_4^s(t_3,t_2,t_1) = \langle\psi(t_3)|^* BU(t_2)|\psi(t_1)\rangle$$

($*$ denotes complex conjugation). In the above formulas, R_1 and R_2 describe evolution of the system in the single-exciton manifold during t_2 and are responsible for the SE contribution. R_3 and R_4 describe evolution of the system in the ground excitonic state during t_2 and are responsible for the GSB contribution.

Appendix B: Double-exciton response functions

The double-exciton response functions $R_1^d - R_4^d$ generated by the four-time response function of Eq. (39) are defined as follows:

$$R_1^d(t_3,t_2,t_1) = \langle g|\langle \mathbf{0}_v\tilde{\mathbf{0}}_v|\hat{\mu}_- e^{iH_\theta t_2}\hat{\mu}_- e^{iH_\theta t_3}\hat{\mu}_+ e^{-iH_\theta(t_1+t_2+t_3)}\hat{\mu}_+|\mathbf{0}_v\tilde{\mathbf{0}}_v\rangle|g\rangle,$$

$$R_2^d(t_3,t_2,t_1) = \langle g|\langle \mathbf{0}_v\tilde{\mathbf{0}}_v|\hat{\mu}_- e^{iH_\theta(t_1+t_2)}\hat{\mu}_- e^{iH_\theta t_3}\hat{\mu}_+ e^{-iH_\theta(t_2+t_3)}\hat{\mu}_+|\mathbf{0}_v\tilde{\mathbf{0}}_v\rangle|g\rangle,$$

$$R_3^d(t_3,t_2,t_1) = \langle g|\langle \mathbf{0}_v\tilde{\mathbf{0}}_v|\hat{\mu}_- e^{iH_\theta t_1}\hat{\mu}_- e^{iH_\theta(t_2+t_3)}\hat{\mu}_+ e^{-iH_\theta t_3}\hat{\mu}_+|\mathbf{0}_v\tilde{\mathbf{0}}_v\rangle|g\rangle,$$

$$R_4^d(t_3,t_2,t_1) = \langle g|\langle \mathbf{0}_v\tilde{\mathbf{0}}_v|\hat{\mu}_- e^{-iH_\theta t_1}\hat{\mu}_- e^{-iH_\theta t_2}\hat{\mu}_+ e^{-iH_\theta t_3}\hat{\mu}_+|\mathbf{0}_v\tilde{\mathbf{0}}_v\rangle|g\rangle.$$

Here R_1^d and R_2^d describe ESA contribution to pump-probe and photon-echo signals, R_3^d and R_4^d are responsible for double-coherence signals [2, 3]. Unfortunately, the double-exciton response functions cannot be expressed in terms of the single-exciton excited-state propagator $A_{\boldsymbol{k}\tilde{\boldsymbol{k}}n}(\tau)$ of Eq. (A4) because the system dynamics during t_3 (R_1^d, R_2^d), t_2+t_3 (R_3^d) and t_2 (R_4^d) develops in the double-exciton manifold. Hence $R_1^d - R_4^d$ should be evaluated on the t_3, t_2, t_1 grid, which is computationally expensive. However, the system propagates during the time interval t_3 in the electronic coherence between the single- and double-exciton manifold (response functions R_1^d and R_2^d) and during the time interval t_2 in the electronic double-coherence between the ground- and double-exciton manifold (response functions R_3^d

and R_4^d). In addition the time interval t_3 corresponds to the electronic coherence between the single- and ground-exciton manifold. Hence its dynamics is controlled by the electronic dephasing, and propagation during t_1, t_3 (R_1^d, R_2^d) and t_1, t_2, t_3 (R_3^d, R_4^d) is controlled by electronic dephasing times which are typically tens of femtosecond for polyatomic species in condensed phase.

Appendix C: Orientational averaging

Following [76, 101, 102], we introduce an orthogonal molecular reference frame with the axes x, y, z specified by three mutually orthogonal unit vectors $\boldsymbol{d}_a$

$$(\boldsymbol{d}_a \boldsymbol{d}_b) = \delta_{ab} \tag{C1}$$

($a = x, y, z$) and decompose vectors of the matrix elements of the transition dipole moments as follows:

$$\boldsymbol{\mu}_n = \sum_{a=x,y,z} \mu_{na} \boldsymbol{d}_a, \tag{C2}$$
$$\mu_{na} = (\boldsymbol{d}_a \boldsymbol{\mu}_n).$$

Then we obtain

$$\hat{\mu}_+ = \sum_{a=x,y,z} (\boldsymbol{s}\boldsymbol{d}_a)\hat{\mu}_+^a, \;\; \hat{\mu}_- = \sum_{a=x,y,z} (\boldsymbol{s}\boldsymbol{d}_a)\hat{\mu}_-^a \tag{C3}$$

where

$$\hat{\mu}_+^a = \sum_n \mu_{na} c_n^\dagger, \;\; \hat{\mu}_-^a = \sum_n \mu_{na} c_n \tag{C4}$$

are the contracted raising and lowering components of the transition dipole moment operators. In the manifold of the single-exciton states defined per Eq. (A1)

$$\hat{\mu}_-^a = |g\rangle\langle e^{(a)}|, \;\; \hat{\mu}_+^a = |e^{(a)}\rangle\langle g| \tag{C5}$$

where

$$|e^{(a)}\rangle = \sum_n \mu_{na} |e_n\rangle. \tag{C6}$$

Let us consider averaging of single-exciton response functions Φ^s. With the definitions of Eqs. (C3) and (C4), the wavefunction $|\psi(\tau)\rangle$ (Eq. (A4)) and the operator B (Eq. (A6)) can be rewritten as follows:

$$|\psi(\tau)\rangle = \sum_{a=x,y,z} (\boldsymbol{s}\boldsymbol{d}_a)|\psi_a(\tau)\rangle,$$

$$B = \sum_{b,c=x,y,z} (\boldsymbol{sd}_b)(\boldsymbol{sd}_c) B_{bc}.$$

Here

$$|\psi_a(\tau)\rangle = e^{-iH_\theta^{(s)}\tau} |\mathbf{0}_v \tilde{\mathbf{0}}_v\rangle |e^{(a)}\rangle, \tag{C7}$$

$$B_{bc} = |e^{(b)}\rangle\langle e^{(c)}| = \sum_{nn'} \mu_{nb}\mu_{n'c} |e_n\rangle\langle e_{n'}|.$$

With this notation,

$$\Phi^s(\tau_4, \tau_3, \tau_2, \tau_1) = \tag{C8}$$

$$\sum_{a,b,c,d} (\boldsymbol{sd}_a)(\boldsymbol{sd}_b)(\boldsymbol{sd}_c)(\boldsymbol{sd}_d) \langle \psi_a(\tau_3 - \tau_4)| B_{bc} U(\tau_3 - \tau_2) |\psi_d(\tau_2 - \tau_1)\rangle.$$

Since $\boldsymbol{d}$-vectors are orthonormal (Eq. (C1)), orientational averaging (denoted by overbar) yields [103]

$$C_{abcd} = \overline{(\boldsymbol{sd}_a)(\boldsymbol{sd}_b)(\boldsymbol{sd}_c)(\boldsymbol{sd}_d)} = \frac{1}{15} \left\{ \delta_{ab}\delta_{cd} + \delta_{ac}\delta_{bd} + \delta_{ad}\delta_{bc} \right\}. \tag{C9}$$

Therefore,

$$\bar{\Phi}^s(\tau_4, \tau_3, \tau_2, \tau_1) = \frac{1}{15} \sum_{a,b} \{ \langle \psi_a(\tau_3 - \tau_4)| B_{bb} U(\tau_3 - \tau_2) |\psi_a(\tau_2 - \tau_1)\rangle$$

$$+ \langle \psi_a(\tau_3 - \tau_4)| (B_{ba} + B_{ab}) U(\tau_3 - \tau_2) |\psi_b(\tau_2 - \tau_1)\rangle \}. \tag{C10}$$

The explicit expressions for double-exciton response functions $\bar{\Phi}^d$ can be obtained analogously.

---

[1] Mukamel, S. Principles of Nonlinear Optical Spectroscopy; Oxford University Press: New York, 1995.

[2] Cho, M. Two-Dimensional Optical Spectroscopy; CRC Press: Boca Raton, 2009.

[3] Valkunas, L.; Abramavicius, D.; Mancal, T. Molecular Excitation Dynamics and Relaxation; Wiley-VCH: Weinheim, 2013.

[4] Domcke, W; Stock, G. Theory of Ultrafast Nonadiabatic Excited-State Processes and their Spectroscopic Detection in Real Time. *Adv. Chem. Phys.* **1997**, 100, 1-169.

[5] Mukamel, S; Abramavicius, D. Many-Body Approaches for Simulating Coherent Nonlinear Spectroscopies of Electronic and Vibrational Excitons. *Chem. Rev.* **2004**, *104*, 2073-2098.

[6] Abramavicius, D; Palmieri, B.; Voronine, D. V.; Sanda, F.; Mukamel, S. Coherent Multidimensional Optical Spectroscopy of Excitons in Molecular Aggreagtes; Quasiparticle vs Supermolecule Perspective. *Chem. Rev.* **2009**, *109*, 2350 - 2408.

[7] Gelin, M. F., Egorova, D. and Domcke, W. Efficient Calculation of Time- and Frequency-Resolved Four-Wave-Mixing Signals. *Acc. Chem. Res.* **2009**, *42*, 1290-1298.

[8] J. Shah, IEEE J. Quant. Electron. **24**, 276 (1988).

[9] M. Gerecke, G. Bierhance, M. Gutmann, N. P. Ernsting, and A. Rosspeintner, Rev. Sci. Instr. **87**, 053115 (2016).

[10] Koppel, H.; Domcke, W.; Cederbaum, L. S. Multimode Molecular Dynamics Beyond the Born-Oppenheimer Approximation. *Adv. Chem. Phys.* **1984**, *57*, 59.

[11] Plasser, F.; Gomez, S.; Menger, M. F. S. J.; Mai, S.; Gonzalez, L. Highly efficient surface hopping dynamics using a linear vibronic coupling model. Phys.Chem.Chem.Phys., 2019, 21, 57

[12] H. D. Meyer, F. Gatti and G. A. Worth, Multidimensional Quantum Dynamics: MCTDH Theory and Applications, Wiley- VCH, Weinheim, 2009.

[13] G. W. Richings, I. Polyak, K. Spinlove, G. A. Worth, I. Burghardt, and B. Lasorne, Int. Rev. Phys. Chem. **34**, 269 (2015).

[14] G. A. Worth, H.-D. Meyer, and L. S. Cederbaum, J. Chem. Phys. 109, 3518 (1998).

[15] A. Raab, G. A. Worth, H.-D. Meyer, and L. S. Cederbaum, J. Chem. Phys. **110**, 936 (1999).

[16] H. Wang, X. Song, D. Chandler, and W. H. Miller, J. Chem. Phys. **110**, 4828 (1999).

[17] H. Wang and M. Thoss, J. Phys. Chem. A 107, 2126 (2003).

[18] I. Kondov, M. Thoss, and H. Wang, J. Phys. Chem. A **110**, 1364 (2006).

[19] H. Wang and M. Thoss. Quantum-mechanical evaluation of the Boltzmann operator in correlation functions for large molecular systems: A multilayer multiconfiguration time-dependent Hartree approach. J. Chem. Phys. 124, 034114 (2006).

[20] R. Borrelli, M. Di Donato, and A. Peluso, J. Chem. Theory Comput. **3**, 673 (2007).

[21] R. Borrelli, M. Di Donato, and A. Peluso, Theor. Chem. Acc. **117**, 957 (2007).

[22] H. Wang and M. Thoss. Nonperturbative simulation of pump–probe spectra for electron transfer reactions in the condensed phase. Chemical Physics Letters 389 (2004) 43–50

[23] H. Wang and M. Thoss, Chem. Phys. **347** (2008) 139-151

[24] B. Bruggemann, P. Persson, H.-D. Meyer, and V. May, Chem. Phys. **347** (2008) 152-165.

[25] T. D. Huynh, K.-W. Sun, M. Gelin, and Y. Zhao, J. Chem. Phys. **139**, 104103 (2013).

[26] K. W. Sun, M. F. Gelin, V. Y. Chernyak, and Y. Zhao, J. Chem. Phys. **142**, 212448 (2015).

[27] K. W. Sun and Y. Yao, J. Chem. Phys. **147**, 224905 (2017).

[28] L. P. Chen, M. F. Gelin, and W. Domcke, J. Chem. Phys. **150**, 024101 (2019).

[29] K. W. Sun, Z. K. Huang, M. F. Gelin, L. P. Chen, and Y. Zhao, J. Chem. Phys. **151**, 114102 (2019).

[30] 4. Sun, K.; Xie, W.; Chen, L.; Domcke, W.; Gelin, M. F. (2020): Multi-faceted spectroscopic mapping of ultrafast nonadiabatic dynamics near conical intersections: A computational study. J. Chem. Phys. 153, 174111.

[31] Sun, K. W.; Xu, Q.; Chen, L. P.; Gelin, M. F.; Zhao, Y. Temperature effects on singlet fission dynamics mediated by a conical intersection. J. Chem. Phys. 153, 194106 (2020).

[32] M. Werther, F. Grossmann, Z.K. Huang, and Y. Zhao, J. Chem. Phys. **150**, 234109 (2019).

[33] M. Werther, S. L. Choudhury, and F. Grossmann, Int. Rev. Phys. Chem. **40**, 81-125 (2020).

[34] Begusic, T.; Vanicek, J. On-the-fly ab initio semiclassical evaluation of time-resolved electronic spectra. *J. Chem. Phys.* **2018**, *149*, 244115.

[35] Begusic, T.; Vanicek, J. On-the-fly ab initio semiclassical evaluation of vibronic spectra at finite temperature. *J. Chem. Phys.* **2020**, *153*, 024105.

[36] Begusic, T.; Vanicek, J. On-the-fly ab initio semiclassical evaluation of third-order response functions for two- dimensional electronic spectroscopy. *J. Chem. Phys.* **2020**, *153*, 184110.

[37] Stock, G.; Thoss, M. Classical description of nonadiabatic quantum dynamics. *Adv. Chem. Phys.* **2005**, *131*, 243.

[38] Uspenskiy, I.; Strodel, B.; Stock, G. Classical Calculation of Transient Absorption Spectra Monitoring Ultrafast Electron Transfer Processes. J. Chem. Theory Comput. 2006, 2, 1605 - 1617.

[39] Gao, X.; Lai, Y.; Geva, E. Simulating Absorption Spectra of Multiexcitonic Systems via Quasiclassical Mapping Hamiltonian Methods. J. Chem. Theory Comput. 2020, 16, 10, 6465-6480.

[40] Gao, X.; Geva, E. A Nonperturbative Methodology for Simulating Multidimensional Spectra of Multiexcitonic Molecular Systems via Quasiclassical Mapping Hamiltonian Methods. J. Chem. Theory Comput. 2020, 16, 10, 6491-6502.

[41] Borrelli, R.; Gelin, M. F. Quantum Electron-Vibrational Dynamics at Finite Temperature:

Thermo Field Dynamics Approach. *J. Chem. Phys.* **2016**, *145*, 224101.

[42] Borrelli, R.; Gelin, M. F. Simulation of Quantum Dynamics of Excitonic Systems at Finite Temperature: an efficient method based on Thermo Field Dynamics. *Sci. Rep.* **2017**, *7*, 9127.

[43] Borrelli R. Theoretical study of charge-transfer processes at finite temperature using a novel thermal Schrödinger equation 2018 Chem. Phys. 515 236-241

[44] Borrelli, R.; Gelin, M. F. Quantum dynamics of vibrational energy flow in oscillator chains driven by anharmonic interactions. 2020 New J. Phys. 22 123002.

[45] H. Umezawa, H. Matsumoto, and M. Tachiki, Thermo field dynamics and condensed states (North-Holland, 1982).

[46] I. Ojima, Annals of Physics 137, 1 (1981).

[47] M. Suzuki, Int. J. Mod. Phys. B 05, 1821 (1991).

[48] Y. Takahashi and H. Umezawa, Int. J. Mod. Phys. B 10, 1755 (1996).

[49] D. S. Kosov, J. Chem. Phys. 131, 171102 (2009).

[50] Oseledets I V 2011 SIAM J. Sci. Comput. 33 2295–317

[51] Haegeman J, Lubich C, Oseledets I, Vandereycken B and Verstraete F Unifying time evolution and optimization with matrix product states 2016 Phys. Rev. B 94 165116

[52] Paeckel S, Köhler T, Swoboda A, Manmana S R, Schollwöck U and Hubig C Time-evolution methods for matrix-product states 2019 Ann. Phys., NY 411 167998.

[53] Finite-temperature density matrix renormalization using an enlarged Hilbert space Adrian E. Feiguin and Steven R. White PHYSICAL REVIEW B 72, 220401 R 2005

[54] Gerhard Ritschel, Daniel Suess, Sebastian M¨obius, Walter T. Strunz, and Alexander Eisfeld. Non-Markovian Quantum State Diffusion for temperature-dependent linear spectra of light harvesting aggregates. J. Chem. Phys., 142(3):034115, 2015.

[55] [28] Ch Sridhar Reddy and M. Durga Prasad. Finite temperature vibronic spectra of harmonic surfaces: A time-dependent coupled cluster approach. Mol. Phys., 113(19-20):3023–3030, 2015.

[56] Chen, L.; Zhao, Y. Finite temperature dynamics of a Holstein polaron: The thermo-field dynamics approach. J. Chem. Phys. 2017, 147, 214102.

[57] Samuel M. Greene and Victor S. Batista. Tensor-Train Split-Operator Fourier Transform (TT-SOFT) Method: Multidimensional Nonadiabatic Quantum Dynamics. J. Chem. Theory Comput. 2017, 13, 4034−4042

[58] Jiajun Ren, Zhigang Shuai, and Garnet Kin-Lic Chan. Time-Dependent Density Matrix Renormalization Group Algorithms for Nearly Exact Absorption and Fluorescence Spectra of Molecular Aggregates at Both Zero and Finite Temperature. J. Chem. Theory Comput. 2018, 14, 5027−5039.

[59] Tong Jiang, Weitang Li, Jiajun Ren,* and Zhigang Shuai. Finite Temperature Dynamical Density Matrix Renormalization Group for Spectroscopy in Frequency Domain. J. Phys. Chem. Lett. 2020, 11, 3761 − 3768

[60] Alberto Baiardi and Markus Reiher. Large-Scale Quantum Dynamics with Matrix Product States. J. Chem. Theory Comput. 2019, 15, 3481−3498.

[61] Xiaoyu Xie, Yuyang Liu, Yao Yao , Ulrich Schollwöck, Chungen Liu, and Haibo Ma. Time-dependent density matrix renormalization group quantum dynamics for realistic chemical systems. J. Chem. Phys. 151, 224101 (2019).

[62] Gaurav Harsha, 1 Thomas M. Henderson, 1,2 and Gustavo E. Scuseria. Thermofield theory for finite-temperature quantum chemistry Cite as: J. Chem. Phys. 150, 154109 (2019).

[63] Sergei Savikhin, Daniel R. Buck, Walter S. Struve. Oscillating anisotropies in a bacteriochlorophyll protein: Evidence for quantum beating between exciton levels. Chemical Physics 223 (1997) 303-312

[64] Maiuri, M.; Ostroumov, E. E.; Saer, R. G.; Blankenship, R. E.; Scholes, G. D. Coherent Wavepackets in the Fenna-Matthews-Olson Complex are Robust to Excitonic-Structure Perturbations Caused by Mutagenesis. Nat. Chem. 2018, 10, 177-183.

[65] Brixner, T.; Stenger, J.; Waswani, H. M.; Cho, M.; Blankenship, R. E.; Fleming, G. R. Two-dimensional spectroscopy of electronic couplings in photosynthesis. Nature 2005, 434, 625-628.

[66] Engel, G. S.; Calhoun, T. R.; Read, E. L.; Ahn, T. -K.; Mančal, T.; Cheng, Y. -C.; Blankenship, R. E.; Fleming, G. R. Evidence for wavelike energy transfer through quantum coherence in photosynthetic systems. Nature 2007, 446, 782-786.

[67] Duan, H.-G.; Prokhorenko, V. I.; Cogdell, R. J.; Ashraf, K.; Stevens, A. L.; Thorwart, M.; Miller, R. J. D. Nature does not rely on long-lived electronic quantum coherence for photosynthetic energy transfer. Proc. Natl. Acad. Sci. USA, 2017, 114 8493-8498.

[68] Thyrhaug, E.; Tempelaar, R.; Alcocer, M. J. P.; Z˘ ídek, K.; Bína, D.; Knoester, J.; Jansen, T. L. C.; Zigmantas, D. Identification and Characterization of Diverse Coherences in the

Fenna-Matthews- Olson Complex. Nat. Chem. 2018, 10, 780.

[69] Scholes, G. D.; Fleming, G. R.; Chen, L. X.; Aspuru-Guzik, A.; Buchleitner, A.; Coker, D. F.; Engel, G. S.; Van Grondelle, R.; Ishizaki, A.; Jonas, D. M.; Lundeen, J. S.; McCusker, J. K.; Mukamel, S.; Ogilvie, J. P.; Olaya-Castro, A.; Ratner, M. A.; Spano, F. C.; Whaley, B.; Zhu, X. Using coherence to enhance function in chemical and biophysical systems. Nature 2017, 543, 647-656.

[70] Mančal, T.; A decade with quantum coherence: How our past became classical and the future turned quantum. Chem. Phys. 2020, 532, 110663.

[71] Cao, J.; Cogdell, R. J.; Coker, D. F.; Duan, H.-G.; Hauer, J.; Kleinekathöfer, U.; Jansen, T. L. C.; Mančal, T.; Miller, R. J. D.; Ogilvie, J. P.; Prokhorenko, V. I.; Renger, T.; Tan, H.-S.; Tempelaar, R,; Thorwart, M.; Thyrhaug, E.; Westenhoff, S.; Zigmantas D. Quantum Biology Revisited. Sci. Adv. 2020; 6: eaaz4888.

[72] Gelin, M. F.; Borrelli, R. Thermal Schrodinger Equation: Efficient Tool for Simulation of Many-Body Quantum Dynamics at Finite Temperature. *Ann. Phys.* **2017**, *529*, 1700200.

[73] Takahashi, Y. & Umezawa, H. Thermo field dynamics. Int. J. Mod. Phys. B 10, 1755–1805 (1996).

[74] T. Meier, V. Chernyak, and S. Mukamel **107**, 8759 (1997).

[75] Zhang, W. M.; Meier, T.; Chernyak, V.; Mukamel, S. J. Chem. Phys. 1998, 108, 7763.

[76] Gelin, M. F.; Borrelli, R.; Domcke, W. Efficient orientational averaging of nonlinear optical signals in multi-chromophore systems. *J. Chem. Phys.* **2017**, *147*, 044114.

[77] Gelin, M. F.; Borrelli, R.; Domcke, W. Origin of Unexpectedly Simple Oscillatory Responses in the Excited- State Dynamics of Disordered Molecular Aggregates. J. Phys. Chem. Lett. 2019, 10, 2806−2810.

[78] Ʊ, ., Ω, ., , ., , . , . ◦|♪ ♪ ♪ ♪ =♪ ∞, ♪ ♪◦|◦ ◦|◦| ♪ ♪∞|◦ ♪† ◦|♪◦|◦ ♪ Ʊ◯. . . ∞. . 2, 3045–3052 (2011).

[79] Adolphs J, M¨ , =∞♪ Ʊ† Ʊ ♪† ♪ 2008 ◦|◦♪ ∞♪ ♪♪ ♪ ♪ Ʊ◯ ♪ ∞ ∞◦|◦ ◦|∞ ♪† ⋆◦|◦♪. . 95 197–209

[80] Tronrud D E, Wen J, Gay L and Blankenship R E 2009 The structural basis for the difference in absorbance spectra for the FMO antenna protein from various green sulfur bacteria Photosynth. Res. 100 79–87

[81] Berman H M, Westbrook J, Feng Z, Gilliand G, Bhat T N, Weissig H, Shindyalov I N and

Bourne P E 2000 The Protein Data Bank Nucl. Acids Res. 28 235–42

[82] S. Mukamel, J. Chem. Phys. 107 (1997) 4165.

[83] Gelin, M. F.; Pisliakov, A. V.; Domcke, W. *Phys. Rev. A* **2002**, *65*, 062507.

[84] Eberly, J. H.; Wodkiewicz, K. *J. Opt. Soc. Am.* **1977**, *67*, 1253.

[85] Mukamel, S.; Ciordas-Ciurdariu, C.; Khidekel, V. *Adv. Chem. Phys.* **1997**, *101*, 345.

[86] Chen, L.; Gelin, M. F.; Zhao, Y.; Domcke, W. Mapping of Wave Packet Dynamics at Conical Intersections by Time-and Frequency-Resolved Fluorescence Spectroscopy: A Computational Study. *J. Phys. Chem. Lett.* **2019**, *10*, 5873 - 5880.

[87] T. Kumpulainen, B. Lang, A. Rosspeintner, and E. Vauthey. Chem. Rev. **117**, 10826 (2017).

[88] Origin of Long-Lived Coherences in Light-Harvesting Complexes Niklas Christensson, Harald F. Kauffmann, T. Pullerits, and T. Mancal J. Phys. Chem. B 2012, 116, 7449 − 7454

⟦89⟧ ♪♪◦|◦♪ ⋆♪◦|◦♪† ♪†= ⋆♪ ♪◦|◦♪ 2◦|◦ ♪◦|◦ ´ ♪, ♪ ♪♪ 2 , †. ♪♪ 2 . ♪♪◦|◦ 1 ◯ 3 2029 2013.

⟦90⟧ , . , Ω. . ♪, . . ♪◦|◦♪◦|◦♪♪◦|◦ ♪◦|◦† ♪ ⋆♪ ♪◦|◦♪ ♪ ◯† †⋆◦|◦. ◦|◦†. ◦|◦ . . . 2013, 110, 1203 − 1208.

⟦91⟧ ◯♪ ♪=† ♪ ◦|◦◦|◦♪† ◦|◦♪ †♪◦|◦ ♪ ♪=♪ ◦|◦ †♪ ♪ 1,2 ♪ Ω♪ 1,3,4◦|◦◦|◦ 637629 ◯ 10.1038/37629

⟦92⟧ ♪†† = ♪† = ♪◦|◦ ◦|◦ ⋆♪◦|◦♪ ♪† ♪◦|◦ ♪ ◦|◦ . ♪† ♪† ♪ . ♪ ⋆. . 2018, 118, 7069 − 7163

⟦93⟧ 7. ♪, . ♪, . ♪, . , . 2020 ♪† ♪=◦|◦ ◦|◦ . . 528, 110495

⟦94⟧ . . ♪, . . †, . . ♪, ♪† . . , . . **99**, 2594 1995.

⟦95⟧ ◦|◦♪=♪, . ♪, . . Ω. ♪ ♪♪=⋆♪ =⋆ ♪ ♪♪†⋆◦|◦† “Ideal” and “real” spectra. *J. Chem. Phys.* **2019**, *150*, 204102.

[96] Borrelli R 2019 Density matrix dynamics in twin- formulation: An efficient methodology based on tensor-train representation of reduced equations of motion J. Chem. Phys. 150 234102

[97] Vibronic origin of long-lived coherence in an artificial molecular light harvester James Lim 1, *, David Palecˇek 2,3, *, Felipe Caycedo-Soler 1 , Craig N. Lincoln 4 , Javier Prior 5 , Hans von Berlepsch 6 , Susana F. Huelga 1 , Martin B. Plenio 1 , Donatas Zigmantas 2 & Ju¨♪ 4 ◯◯◯ 67755 ◯ 10.1038/♪◦|◦8755 .♪◦|◦/♪◦|◦♪◦|◦♪ 1 201

⟦98⟧ †=♪†◦|◦† ♪ ♪ =♪♪=◦|◦ ◦|◦♪◦|◦ †♪ ◯◯◦|◦ , †,‡ ♪, ¶,§ . ♪♪, ¶,§ ⋆◦|◦ † ♪† ♪ ♪♪∗ ,†,‡.

. . . 2016, 7, 277–282

[[99]] 148, 174102 2018 † 10.1063/1.5026753

[[100]] . . 153, 204109 2020 //†./10.1063/5.0027962 01 2020 . 06 2020 . 25 2020

[[101]] . , . , . , †íguez, New J. Phys. **14**, 023018 (2012).

[102] C. Brüning and V. Engel. Chem. Phys. **482**, 64 (2017).

[103] R. M. Hochstrasser, Chem. Phys. **266**, 273 (2001).